Lab on a Chip

Devices and applications at the micro- and nanoscale

rsc.li/loc

ROYAL SOCIETY
OF **CHEMISTRY**

PAPER
Woon-Hong Yeo *et al.*
Capillary-driven, superhydrophilic microfluidic retainer for
continuous salivary glucose monitoring

25 YEARS
ANNIVERSARY

Check for updates

Capillary-driven, superhydrophilic microfluidic retainer for continuous salivary glucose monitoring

Jimin Lee, [ID] [ab] JunHo Song, [c] Juo Kim, [c] Arianna Lee, [ID] [d] Saewoong Oh, [ID] [ab] Beomjune Shin, [ID] [ab] Kyoungmin Min [ID] [c] and Woon-Hong Yeo [ID] *[abefg]

Salivary glucose monitoring provides a non-invasive alternative to blood-based diabetes tests; however, low analyte levels and unstable microfluidic wetting have hindered its translation. Here, we introduce a retainer-based microfluidic system that integrates a capillary-driven, superhydrophilic microchannel with a miniaturized three-electrode enzymatic sensor for continuous salivary glucose monitoring. This device maintains sustained hydrophilicity for at least 120 days without compromising flexibility or biocompatibility. The gold working electrode, functionalized with glucose oxidase immobilized in a carbon nanotube–chitosan matrix and a thin glutaraldehyde overlayer, offers sensitive and stable detection. The integrated sensor shows a chronoamperometric sensitivity of 15.48 $\mu A\ mM^{-1}\ cm^{-2}$ and a limit of detection of <42 μM. The *in vitro* measurements using glucose-spiked artificial saliva show the reproduced postprandial profiles with rapid signal stabilization and high run-to-run repeatability over three cycles. Overall, this work captures the potential of the retainer-based microfluidic system as a practical pathway toward continuous, non-invasive salivary glucose monitoring.

Introduction

Diabetes mellitus is a global health challenge, currently affecting over 589 million people and projected to surpass 853 million by 2050.[1] Effective disease management depends on frequent monitoring of blood glucose to prevent microvascular and macrovascular complications, including neuropathy, retinopathy, nephropathy, and cardiovascular disease.[2] Although fingerstick glucometers and continuous glucose monitors are effective, they remain invasive, can be painful, and are poorly tolerated in pediatric and long-term use.[3–6] These

limitations have catalyzed interest in non-invasive monitoring with saliva emerging as an attractive biofluid due to its ease of collection, mirroring of blood-glucose trends, and ability to be sampled continuously in the oral cavity.[7–9] The central challenge is twofold: salivary glucose is $\sim100\times$ lower than in blood (typically ~1–$10\ mg\ dL^{-1}$; ~0.06–$0.56\ mM$), and microfluidic interfaces used to collect and route saliva lose hydrophilicity over time, undermining capillary transport.[10–12]

Polydimethylsiloxane (PDMS) is the most widely used substrate for fabricating microfluidic channels due to its low cost, ease of prototyping *via* soft lithography, optical transparency, flexibility, and biocompatibility, which make it particularly suitable for rapid prototyping and biomedical applications.[13–15] Conventional strategies to render PDMS hydrophilic, such as oxygen-plasma activation and surfactant coatings (*e.g.*, Triton X-100), are transient or leachable. Plasma-treated surfaces reorganize and revert toward hydrophobicity within days, while surfactants can desorb, foul sensors, and complicate biocompatibility.[16–18] Thus, a durable, maintenance-free hydrophilic interface is a prerequisite for the practical, capillary-driven sampling of oral fluids.[19]

To achieve long-term capillary flow within an intraoral device, we adopted a bulk-modified PDMS composite based on poly(dimethylsiloxane-*b*-ethylene oxide) (PDMS-*b*-PEO). Unlike conventional hydrophilic strategies—such as PEG,[20–23] PVA,[24–26] Pluronic F127,[27–29] or hyaluronic-acid[30–32] coatings—which typically require plasma activation, multi-step grafting, or

[a] George W. Woodruff School of Mechanical Engineering, Georgia Institute of Technology, Atlanta, GA 30332, USA
[b] Wearable Intelligent Systems and Healthcare Center (WISH Center) at the Institute for Matter and Systems, Georgia Institute of Technology, Atlanta, GA 30332, USA
[c] School of Mechanical Engineering, Yonsei University, 50 Yonsei-ro, Seodaemun-gu, Seoul 03722, Republic of Korea
[d] School of Electrical and Computer Engineering, Georgia Institute of Technology, Atlanta, GA 30332, USA
[e] Wallace H. Coulter Department of Biomedical Engineering, Georgia Institute of Technology and Emory University School of Medicine, Atlanta, GA 30332, USA
[f] Parker H. Petit Institute for Bioengineering and Biosciences, Georgia Institute of Technology, Atlanta, GA 30332, USA
[g] Korea KIAT-Georgia Tech Semiconductor Electronics Center (K-GTSEC) at the Institute for Matter and Systems, Georgia Institute of Technology, Atlanta, Georgia 30332, USA

immersion-assisted activation and still suffer from hydrophobic recovery or coating delamination, PDMS-*b*-PEO provides a structurally integrated approach. The PDMS segment covalently crosslinks within the Sylgard 184 matrix, preserving elasticity and dimensional stability, while the PEO segment spontaneously enriches the surface, yielding persistent hydrophilicity for over 120 days without re-treatment. Recent work has noted that although polymeric surface coatings can extend PDMS wettability, these methods generally involve complex thermal and temporal control and maintain hydrophilicity only for several weeks. In contrast, PDMS–(PDMS-*b*-PEO) functions as a single-step bulk additive that resists leaching, maintains optical and mechanical integrity, and enables durable capillary-driven saliva transport within intraoral microchannels, making it particularly well-suited for long-term retainer-based sensing systems.

Recent comprehensive reviews on wearable and noninvasive glucose sensing have emphasized that saliva, while an attractive biofluid, is an analytically demanding matrix requiring high sensitivity within the 0.05–1.0 mM range, rigorous selectivity against endogenous interferents, and reproducible performance in realistic oral-like environments.[33–35] Salivary and oral glucose platforms such as toothbrush-based electrochemical sensors and mouthguard biosensors have demonstrated linear ranges matched to physiological salivary glucose levels and highlighted the importance of validating selectivity, storage stability, and matrix effects using artificial saliva or phantom jaw models. These benchmarks collectively establish the analytical criteria necessary for reliable salivary glucose monitoring and inform the design of the present retainer-based sensing system.

In this work, we report a retainer-format intraoral microfluidic sensing platform built on a bulk-modified PDMS–(PDMS-*b*-PEO) composite that sustains superhydrophilicity (*i.e.*, <20° contact angle) without plasma treatment or surfactants. Incorporation of ≤5 wt% amphiphilic block copolymer enriches PEO segments at the surface, yielding stable water contact angles (<20°) over extended storage while maintaining flexibility and bio-inertness. Microchannels patterned by laser micromachining are integrated into a 3D-printed orthodontic form factor, enabling capillary-driven saliva transport to an electrochemical glucose sensor. The system demonstrates real-time, continuous salivary glucose tracking under dynamic conditions. Besides glucose, this material-driven strategy establishes a versatile framework for non-invasive biofluid monitoring. The capillary-driven, superhydrophilic thin-film design can be adapted for low-abundance analytes in sweat, tears, nasal mucus, or interstitial-fluid surrogates, enabling stable and maintenance-free operation in wearable or oral devices. By addressing the longstanding limitation of PDMS hydrophobic recovery, our platform provides a practical foundation for continuous salivary glucose monitoring and broadens the landscape of retainer-based biofluid diagnostics.

Experimental

Materials

The polydimethylsiloxane (PDMS, Sylgard 184) base and curing agent were purchased from Dow Corning. The poly(dimethylsiloxane-*b*-ethylene oxide) block copolymer (PDMS-*b*-PEO, methyl terminated) was acquired from Polysciences Inc. Multi-walled carbon nanotubes (MWCNTs, >95%, carboxyl-functionalized), glucose oxidase (GOx, from *Aspergillus niger*, 250 000 units), chitosan (medium molecular weight), glutaraldehyde (25% aqueous solution), Nafion (5% solution), and phosphate-buffered saline (PBS, 1×, pH 7.4) were sourced from Sigma-Aldrich. Artificial saliva (Fusayama–Meyer formulation) and D-(+)-glucose (99%, Sigma-Aldrich) were used for *in vitro* testing. All solvents were of analytical grade. Cellulose-based wicking pads (thickness 0.83 mm, Sigma-Aldrich) were used in vent/outlet assemblies. Dental-grade biocompatible photopolymer resin (low-shrinkage 3D printer resin) for the retainer frame was sourced from RESIONE.

Simulation model construction

To investigate the wetting behavior of PDMS and PDMS-*b*-PEO, molecular dynamics (MD) simulations were performed using the large-scale atomic/molecular massively parallel simulator (LAMMPS).[36] Recent studies have reported that PDMS-*b*-PEO undergoes surface rearrangement upon exposure to water, whereby the hydrophilic PEO block becomes enriched at the outermost surface and the PDMS block is no longer exposed at the interface.[37] To emulate this fully surface-segregated state and isolate the intrinsic contribution of the hydrophilic block, a neat PEO substrate was used instead of explicitly constructing the PDMS-*b*-PEO copolymer. Consequently, the wetting behavior of water on PDMS and PEO substrates was directly compared. Interfacial simulations were carried out using water droplets in contact with PDMS and PEO substrates. The water droplet was modeled as a nanocluster composed of 3776 molecules, forming an initial spherical droplet with a radius of 3 nm. The separation between the bottom of the droplet and the substrate was initially set to 0.3 nm.[38] Both PDMS and PEO substrates were generated as amorphous structures using Materials Studio. For PDMS, the degree of polymerization was set to 25, exceeding the critical chain length (n_c = 20 units).[39] The PDMS substrate dimensions were 12.0 nm in length and 3.3 nm in thickness.[40] A total of 150 PDMS chains were used, and the mass density was fixed at 0.965 g cm^{-3}, consistent with experimental reports.[41] For PEO, the polymer chains were terminated with methyl groups, and the degree of polymerization was matched to that of PDMS. The PEO substrate dimensions were 10.6 nm in length and 3.3 nm in thickness. The number of PEO chains was set to 180, and the initial density was fixed at 0.95 g cm^{-3}. This is lower than the experimental bulk density of 1.20 g cm^{-3},[42] because direct construction at the experimental value resulted in severe bond overlap during amorphous cell generation. Thus, the

PEO amorphous cell was first created at a slightly reduced density and subsequently relaxed toward the experimental density during equilibration.

Force field description and simulation methodology

To describe the interatomic interactions in the PDMS and PEO systems, the optimized potentials for liquid simulations (OPLS) all-atom force field was employed.[43,44] Water droplets were modeled using the SPC/E water model.[45] To simulate the solid–liquid interface within this hybrid force-field framework, non-bonded cross-interactions between dissimilar atom types were computed using the Lorentz–Berthelot (LB) mixing rule.[46] Lennard–Jones interactions used a cutoff distance of 11.0 Å, and the switching distance for long-range electrostatics was also set to 11 Å. The equations of motion were integrated using the velocity-Verlet algorithm with a time step of 1.0 fs. During canonical (NVT) ensemble simulations, the temperature was controlled using a Nosé–Hoover thermostat with a damping time of 100 fs. Each system was initially relaxed by minimizing the configuration using the conjugate-gradient (CG) algorithm to remove local stress in both the water droplet and the substrate. After equilibration, the substrates were fixed as rigid bodies to prevent further structural rearrangement. Periodic boundary conditions were applied in the x and y directions, while a non-periodic, shrink-wrapped boundary with a 10.0 nm vacuum layer was used along the z direction. Once system energies had stabilized, the substrate–water interface was reconstructed, and the combined system was further simulated for 1 ns in the NVT ensemble at 300 K. The water contact angle on PDMS was determined by fitting a circle to the droplet profile and drawing a tangent line at the interface.[47] Measurements were obtained across multiple cross-sectional planes, and the mean value with standard deviation was reported.

Fabrication of PDMS–(PDMS-b-PEO) composite films

PDMS-b-PEO was blended into PDMS at 0.1–5.0 wt% relative to the combined mass of the PDMS base + curing agent (10:1 w/w base:curing ratio). For each batch, the required mass of PDMS-b-PEO was pre-dispersed in the PDMS base by gentle hand mixing for 10 min to reduce viscosity, and then the curing agent was added. The prepolymer was mixed homogeneously for an additional 5 min, followed by vacuum degassing for 30 min to collapse trapped air bubbles. Films were cast solvent-free into a spacer-defined mold consisting of a parylene-coated flat substrate. The films (~600 μm thickness) were cast with a doctor blade and leveled for 5 min. Curing was performed at 80 °C for 1 h, followed by post-curing at 110 °C for 1 h to complete crosslinking and promote surface PEO enrichment. After demolding, films were optionally pre-rinsed in isopropyl alcohol for 30 min and dried at 65 °C to remove any non-bound amphiphiles prior to laser patterning. Final films were stored in a desiccator (22 ± 2 °C, 30–40% RH) until use. Optical opacity, mechanical flexibility, and hydrophilicity (via dynamic contact angle) were characterized post-curing.

Microchannel patterning via laser micromachining

Cured PDMS–(PDMS-b-PEO) films (600 μm thick) were patterned by successive laser pyrolysis (SLP) on an OPTEC micromachining system. Channel networks (inlet, prefilter, sensor window, vents/outlet) were defined at 100–500 μm nominal widths (main channels ~300 μm) and registered to the sensor features. Oxygen-plasma or surfactant treatment was not used at any stage. After patterning, residues were removed by brief ultrasonic cleaning in isopropyl alcohol, and parts were dried at 65 °C. The channel width/depth was verified by optical profilometry.

Retainer design and integration

Custom-fit orthodontic retainers were designed in SolidWorks based on standard human palate models and 3D printed using biocompatible dental resin. Laser-patterned PDMS–(PDMS-b-PEO) films were adhesively bonded to recessed grooves within the retainer using uncured PDMS as a bonding layer and cured at 80 °C for 1 h. Final assemblies were visually inspected and tested for capillary-driven flow.

Electrochemical glucose sensor fabrication

The electrochemical sensor consisted of: (1) a working electrode (WE): a gold film (100 nm Au/10 nm Ti) on thin-film PI with Cu traces, modified with GOx (2 mg mL^{-1}) embedded in a chitosan (0.5% w/v) + MWCNT (1 mg mL^{-1}) matrix, crosslinked with 0.5% glutaraldehyde; (2) a reference electrode (RE): electroplated and subsequently chlorinated Ag/AgCl on a bare gold film + PVB/KCl; (3) a counter electrode (CE): an electroplated gold film. After functionalization, sensors were stored at 4 °C for 24 h prior to testing. The limit of detection (LOD) was determined based on the signal-to-noise criterion (S/N = 3), calculated as:

$$LOD = 3\sigma/m \tag{1}$$

where σ represents the standard deviation of the baseline current and m is the calibration slope. For a 2 mm-diameter working electrode (geometric area = 0.0314 cm^2), the baseline noise was measured to be approximately 6–7 nA, corresponding to 0.217 μA cm^{-2} when normalized by the electrode area.

Hydrophilicity and mechanical characterization

Static water contact angle measurements were performed using a goniometer (Model 250 Goniometer with DROPimage Advanced, ramé-hart) at days 0, 30, and 120 under ambient dry conditions. Stress–strain curves were obtained using a tensile tester (Mark-10 Series 5 force meter, ESM303) with a film width of 5 mm, a gauge length of 30 mm, and a strain rate of 5 mm min^{-1}. Swelling experiments were conducted by immersing samples in artificial saliva at 37 °C, measuring mass and thickness changes over 90 days. The cross-sectional morphology of the electrochemical working electrode was examined using field-emission scanning electron microscopy

(FE-SEM, SU8230, Hitachi) to confirm uniformity of the multilayered matrix. Fourier-transform infrared spectroscopy (FTIR, Nicolet IS50, Thermo Scientific) and X-ray photoelectron spectroscopy (XPS, Thermo K-Alpha XPS, Thermo Scientific) were employed to evaluate the chemical composition and surface characteristics of PDMS–(PDMS-*b*-PEO) composites, verifying successful incorporation of PEO segments and surface enrichment.

In vitro salivary glucose monitoring

The integrated device was placed in a custom-built saliva reservoir chamber filled with artificial saliva spiked with glucose (0.01–25 mM) to simulate physiological fluctuations. Chronoamperometric measurements were conducted using a potentiostat (Interface 1010 E, Gamry Instruments) at +0.45 V *vs.* Ag/AgCl. Stepwise glucose injections were applied, and the corresponding current responses were recorded. Signal repeatability, drift, and response time were evaluated over three cycles. Data are presented as the mean ± standard deviation (SD). Statistical analyses and curve fitting (*e.g.*, Cottrell analysis) were performed using Echem AnalystTM Software and OriginPro 2022.

Results and discussion

Overview of the system

Fig. 1 provides an overview of the proposed retainer-based platform for continuous salivary glucose monitoring. We selected an orthodontic retainer architecture as the intraoral form factor (Fig. 1A), as this configuration is familiar and minimally intrusive, and can be fabricated to fit precisely within an individual's oral cavity.[48–50] The retainer body was 3D printed using a biocompatible resin, providing a rigid yet comfortable base for integration.[51] A key advantage of this structure is the ability to incorporate a thin polymeric microchannel membrane
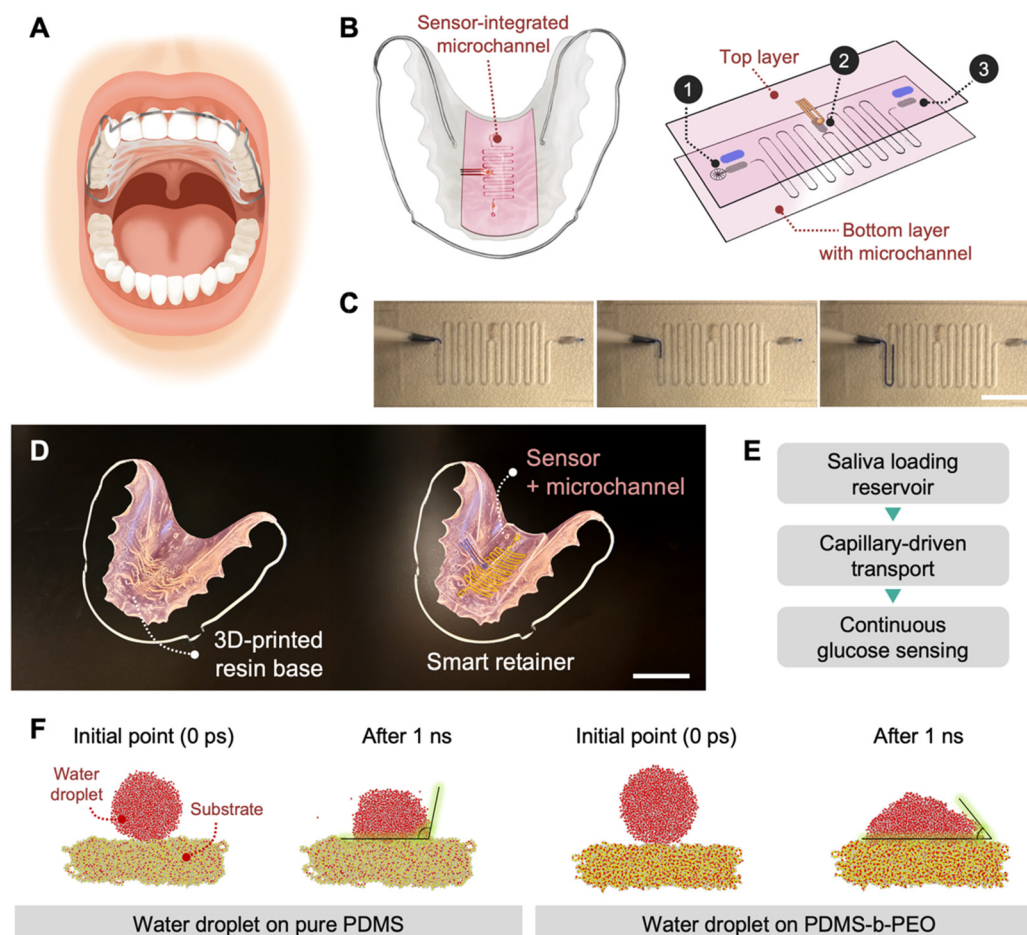

Fig. 1 Concept and design of the retainer-based salivary glucose monitoring platform. (A) Schematic illustration of an orthodontic retainer positioned intraorally, enabling direct saliva sampling into embedded microchannels. (B) Exploded-view diagram showing structural components: resin retainer base, laser-patterned PDMS–(PDMS-*b*-PEO) microchannel layer, and integrated electrochemical glucose sensor. (C) Time-lapse images of capillary-driven saliva transport within the fabricated microchannel, showing spontaneous filling and flow continuity. (D) Photograph of the fabricated orthodontic retainer prototype. (E) Workflow diagram summarizing the operational principle: saliva loading, capillary-driven transport, and continuous electrochemical glucose sensing. (F) Contact angle measurement using MD simulations; initial and 1 ns configurations of a water droplet on pure PDMS (left); initial and 1 ns configurations of a water droplet on the PDMS-*b*-PEO block copolymer substrate (right).

and an electrochemical glucose sensor directly onto the resin frame, enabling seamless integration without bulky external components (Fig. 1B).[52–54] The microchannel was designed to include (1) a saliva inlet, (2) a reservoir region accommodating the electrochemical sensor, and (3) a vent/outlet connected to cellulose-based wicking pads to facilitate continuous flow. The inlet–reservoir–wicking architecture generates a unidirectional capillary pressure gradient that prevents reverse flow and suppresses bubble formation during steady saliva intake. This configuration distinguishes the present platform from conventional hydrophilic PDMS microfluidics that rely on external injection or plasma-treated channels with transient wettability. As demonstrated in Fig. 1C, dyed artificial saliva spontaneously filled the channel network *via* capillary action, confirming smooth transport and connectivity between compartments. A comparison between a conventional orthodontic retainer and the proposed "smart retainer" (Fig. 1D) highlights the minimal visual footprint of the integrated design, avoiding protruding wires or external housings that could compromise comfort and wearability. While full integration of wireless measurement circuitry, as demonstrated by Lee *et al.*, is feasible, the present study focuses on the feasibility of microchannel–sensor integration, with electronic integration to be addressed in future work.[55] The functional workflow is summarized in Fig. 1E: saliva is continuously collected into the microchannel by capillary-driven flow, delivered to the sensing region, and analyzed in real time by the embedded electrochemical glucose sensor. However, conventional PDMS, widely used for microfluidic channel fabrication, is intrinsically hydrophobic, limiting spontaneous wetting and capillary transport.[56,57] To overcome this limitation, prior studies have employed oxygen plasma treatment or chemical coatings to temporarily increase surface hydrophilicity.[58,59] These approaches, however, suffer from limited stability with rapid hydrophobic recovery. To address this challenge, we adopted a material-level strategy by blending PDMS with a small fraction of poly(dimethylsiloxane-*b*-ethylene oxide) (PDMS-*b*-PEO), a biocompatible amphiphilic block copolymer. Incorporation of PEO domains imparts durable hydrophilicity while maintaining the mechanical flexibility and biocompatibility of PDMS.[60] Prior reports have shown that such composites can sustain surface hydrophilicity for over 120 days.[61] Nonetheless, their application to functional microchannels for intraoral fluidics, coupled with systematic analyses of long-term surface stability, has not been comprehensively investigated. Therefore, we performed molecular dynamics simulations to compare the wetting behavior of conventional PDMS with that of PDMS-*b*-PEO. Fig. 1F presents the wetting behavior of PDMS and PDMS-*b*-PEO from the initial point to 1 ns, along with the corresponding interaction energies and contact angles. As shown in Fig. S1, the contact angle of PDMS was measured to be 98.23° ± 2.249, which is consistent with experimentally reported values of 101° to 120°.[62] By contrast, the contact angle of PDMS-*b*-PEO was determined to be 38.63° ± 5.024. It remains reasonable given that the block copolymer structure combining PDMS and PEO

is between 21.5 and 80.9°.[60] Since no direct chemical bonding exists between water molecules and the substrates, our analysis focused on non-bonded interactions, including hydrogen bonding and van der Waals (vdW) interactions. Accordingly, the interaction energy between the water droplet and the PDMS substrate was evaluated to quantify the non-bonded interactions at the solid–liquid interface. The interaction energy was calculated using the following expression:

$$E_{interaction} = E_{total} - (E_{substrate} + E_{water}) \qquad (2)$$

where E_{total} is the total energy of the water droplet–substrate system, $E_{substrate}$ is the energy of the substrate in the absence of the droplet, and E_{water} represents the energy of the isolated water droplet. As shown in Fig. S1, the interaction energy analysis further confirmed that PEO (-1546.249 kcal mol^{-1}) exhibits a substantially lower interaction energy compared to PDMS (-477.272 kcal mol^{-1}), indicating a stronger affinity toward water molecules. To provide further insight into the intermolecular interactions, the radial distribution function (RDF) was examined, as shown in Fig. S2. For this analysis, only the interfacial region within 20 Å of the PDMS/water and PEO/water droplets was considered after 1 ns of MD simulation. In systems where no chemical bonding occurs, it is well established that the region between 1.1 and 3.1 Å corresponds to hydrogen bonding, whereas the 3.1–5.0 Å range primarily reflects van der Waals (vdW) and electrostatic interactions.[63] Accordingly, RDFs were analyzed within the distance range of 1.0–6.0 Å. The oxygen and hydrogen atoms in the water droplet are denoted as O and H (from H_2O), respectively. Aside from the O–H(H_2O) hydrogen-bonding correlation, no distinct peaks were observed in the PDMS–water RDFs, and the overall peak intensities appeared broad and weak. This indicates that PDMS forms no significant non-bonded interactions with the water droplet, consistent with its higher (less favorable) interaction energy relative to PEO. In contrast, the PEO–water O–H(H_2O) correlation exhibits a much sharper and more intense peak at approximately 2.73 Å, while the O–O(H_2O) correlation also displays a pronounced peak near 3.69 Å. These features align with previous reports demonstrating that ether oxygens in PEO readily form strong hydrogen bonds with water molecules.[64] Such enhanced interactions confirm that PEO displays markedly higher hydrophilicity than PDMS. This stronger interfacial interaction directly contributes to the significantly smaller contact angle of water on PEO relative to PDMS. Collectively, atomistic molecular dynamics simulations clearly demonstrate that introducing PEO effectively transforms the intrinsically hydrophobic PDMS surface into a more hydrophilic interface, owing to the substantially stronger intermolecular interactions between PEO and water molecules.

Stable hydrophilicity and mechanical integrity of PDMS–(PDMS-*b*-PEO) composites

We next examined the physicochemical and mechanical properties of PDMS–(PDMS-*b*-PEO) composites across a range of

PEO concentrations (0.1–5.0 wt%). Fig. 2A illustrates the amphiphilic structure of PDMS-*b*-PEO, composed of a hydrophobic PDMS backbone and hydrophilic PEO blocks. Bulk incorporation of PDMS-*b*-PEO into PDMS led to visibly increased opacity with higher PEO loading, indicating microphase separation and dispersed PEO domains.[60,65] The XPS spectra show a progressive increase in the O 1s signal with higher PEO loading (Fig. 2B). To quantitatively support this trend, the corresponding O/C ratios are directly shown within the figure. These ratios increase from 1.367 for 1.0 wt% PDMS-*b*-PEO to 1.585 for 5.0 wt% PDMS-*b*-PEO, clearly reflecting the compositional enrichment of PEO at the film surface as the block-copolymer content increases (see each elemental result and O/C ratio at different PDMS-*b*-PEO levels in Fig. S3). These findings verify that PEO segments were successfully incorporated and enriched at the composite surface (see the FTIR spectra in Fig. S4). Hydrophilicity was evaluated by contact

angle measurements. Representative droplet images at day 0 and day 120 (Fig. 2C) highlight the difference between pristine PDMS and PEO-modified composites. Pure PDMS remained hydrophobic, whereas composites containing PEO demonstrated rapid droplet spreading and long-term wetting stability. Quantitative measurements (Fig. 2D) showed that films with 3.0–5.0 wt% PEO maintained superhydrophilic surfaces with contact angles below 20° for up to 120 days under ambient storage conditions, while oxygen plasma-treated PDMS quickly reverted to hydrophobicity within just a few hours. The contrast is further visualized in Movie S1, where droplets on pristine PDMS retained a spherical shape after 10 seconds, while those on PDMS–(PDMS-*b*-PEO) substrates flattened completely, demonstrating the persistence of hydrophilicity. Mechanical performance was assessed by uniaxial tensile testing. As shown in Fig. 2E, composites containing up to 3.0 wt% PEO retained the intrinsic elasticity of PDMS, with Young's modulus values of
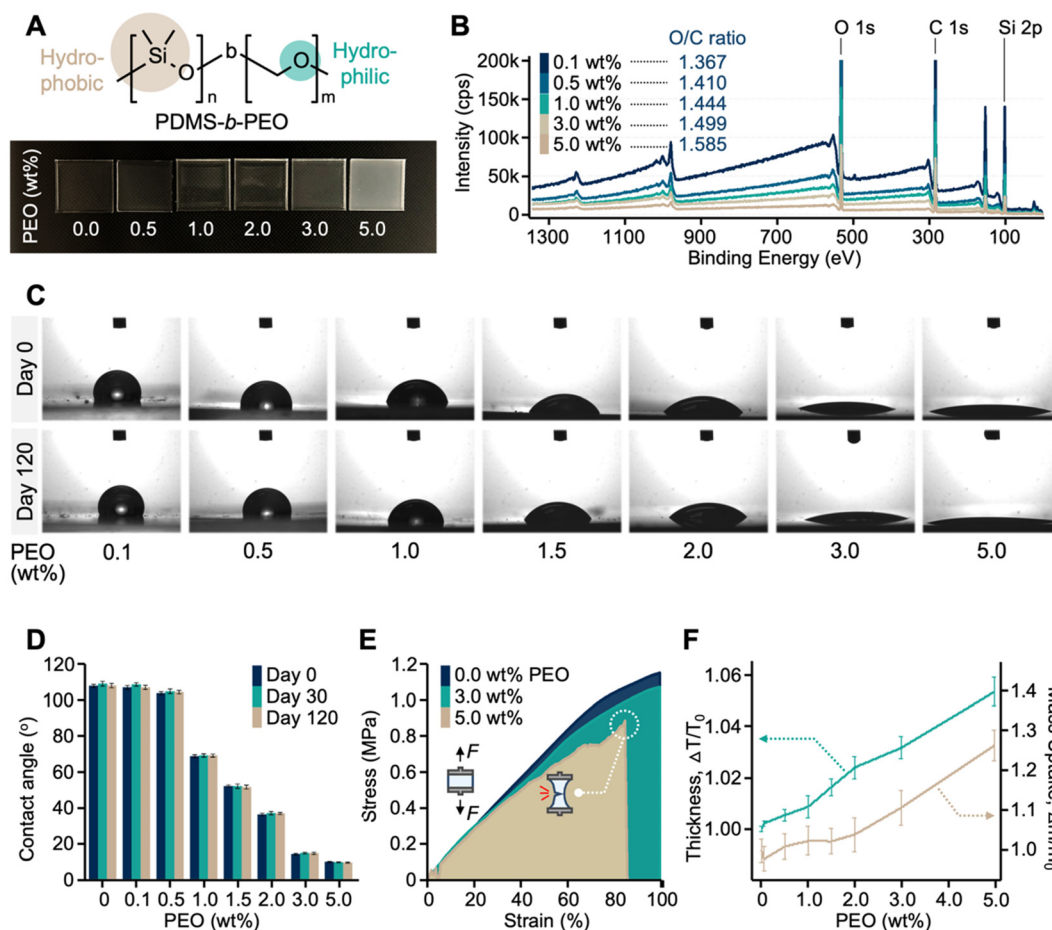

Fig. 2 Amphiphilic and functional properties of PDMS–(PDMS-*b*-PEO) composites. (A) General molecular structure of the PDMS-*b*-PEO copolymer, exhibiting amphiphilic characteristics with hydrophobic PDMS and hydrophilic PEO blocks (top); optical images of PDMS–(PDMS-*b*-PEO) composites showing increased opacity with higher PEO content (bottom). (B) XPS spectra of composites with varying PDMS-*b*-PEO concentrations, confirming incorporation of PEO domains, and corresponding elemental signals (O 1s, C 1s, and Si 2p). (C) Representative water contact angle images at day 0 and day 120 across different PEO concentrations (0.1–5.0 wt%). (D) Quantified contact angle values over time (days 0, 30, and 120), measured under dry storage conditions, showing enhanced and sustained hydrophilicity with increasing PDMS-*b*-PEO content. (E) Stress–strain curves of composites with different PDMS-*b*-PEO concentrations, indicating reduced mechanical stretchability at ≥5.0 wt% PEO (film rupture observed with notched samples). (F) Swelling behavior after 90 day immersion in artificial saliva: normalized thickness change ($\Delta T/T_0$, left axis) and normalized mass uptake ($\Delta m/m_0$, right axis) increase with PEO concentration, confirming partial water absorption by PEO domains.

around 1.2 MPa and fracture strains exceeding 100%.[66,67] At higher PEO contents (≥5.0 wt%), however, the films exhibited embrittlement and premature rupture under tensile stress, indicating that excessive PEO incorporation compromises mechanical reliability. Swelling stability was further examined by immersing samples in artificial saliva at 37 °C for 90 days. The results, shown in Fig. 2F, revealed a gradual increase in both mass uptake and thickness expansion with increasing PEO concentration.[68] At 3.0 wt% PEO, the normalized mass uptake ($\Delta m/m_0$) reached approximately 10%, with a corresponding thickness increase of $\Delta T/T_0 \approx 1.03$. These moderate changes confirm partial hydration of PEO segments but did not disrupt the overall dimensional stability of the films, ensuring compatibility with rigid dental substrates. Collectively, these results demonstrate that PDMS–(PDMS-b-PEO) composites provide a material platform with stable hydrophilicity,

mechanical robustness, and controlled swelling suitable for long-term intraoral use.[69,70] To more clearly compare the behavior of different formulations, Table S1 summarizes the hydrophilicity, mechanical properties, swelling characteristics, and microchannel patternability across all tested PEO loadings (0.1–5.0 wt%). As shown in this comparative analysis, the 3.0 wt% composition uniquely balances persistent wettability, elasticity, dimensional stability, and manufacturability, thereby emerging as the optimal formulation for reliable intraoral microfluidic integration.

Glucose sensor performance

The electrochemical glucose sensor was designed around a glucose oxidase (GOx)-based enzymatic mechanism (Fig. 3A; see the dimensions of the electrodes and laser patterning sequence
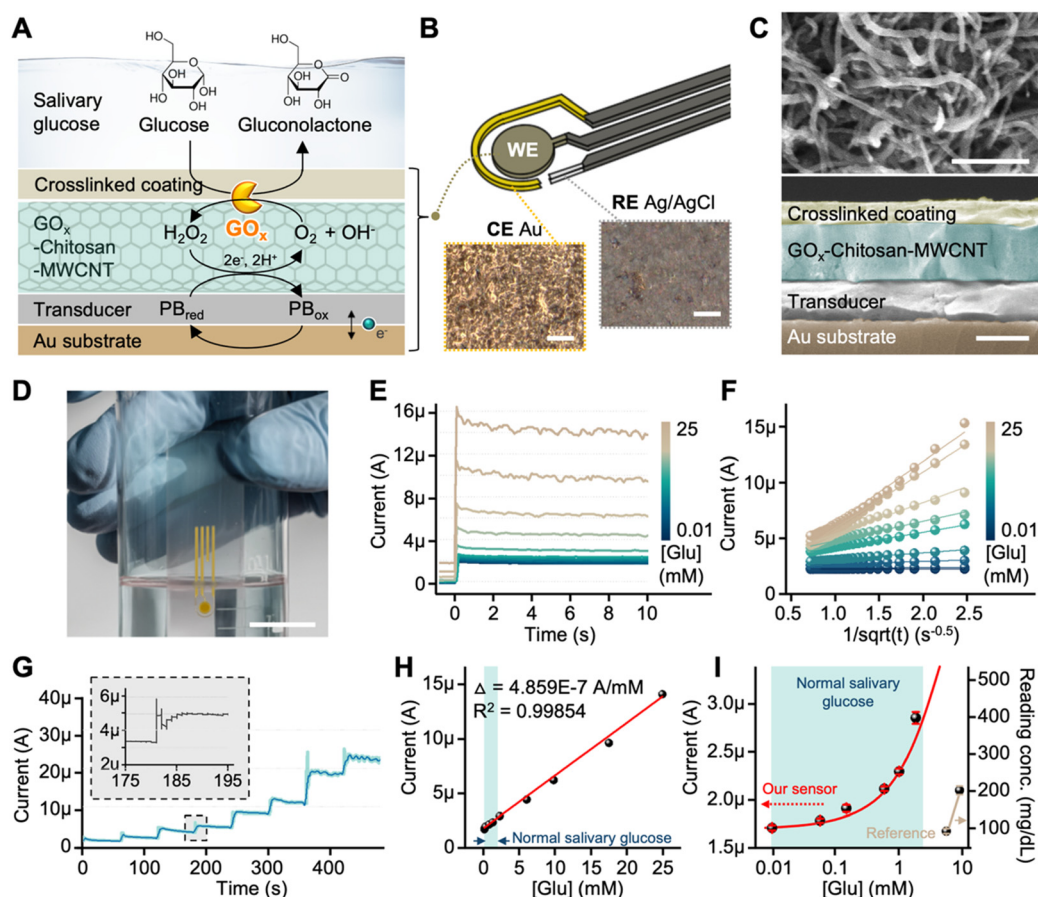

Fig. 3 Structural design and electrochemical performance of the salivary glucose sensor. (A) Schematic illustration of the glucose oxidation and detection mechanism at the GOx-based working electrode. Glucose is catalytically oxidized to gluconolactone, generating H₂O₂, which is further decomposed to release electrons for signal transduction. (B) Configuration of the three-electrode system (working (WE), reference (RE), and counter (CE) electrodes), with corresponding optical micrographs of the RE and CE. Scale bar = 50 μm. (C) (Top) FE-SEM image of the multi-walled carbon nanotube (MWCNT) network structure; (bottom) cross-sectional SEM image of the working electrode, revealing layered construction: Au substrate, transducer, GOx–chitosan–MWCNT, and crosslinked glutaraldehyde coating. Scale bar = 500 nm. (D) Photograph of the experimental setup used for calibration, showing the electrode immersed in glucose stock solutions. Scale bar = 2 cm. (E) Chronoamperometric current responses corresponding to various glucose concentrations (0.01–25 mM), demonstrating signal magnitude increases with glucose levels. (F) Cottrell analysis of transient current profiles, used to extract diffusion coefficients from τ values. (G) Real-time chronoamperometric trace during stepwise glucose injections, showing discrete current steps. (H) Calibration curve derived from steady-state current *vs.* glucose concentration. (I) Magnified view of the calibration curve, highlighting the physiological range of normal salivary glucose for comparison and sensor validation.

provided in Fig. S5 and Movie S2, respectively). Glucose was catalytically oxidized to gluconolactone, producing H_2O_2 as the measurable intermediate.[71–73] To ensure long-term stability of the enzymatic layer, a glutaraldehyde-based crosslinked coating was applied, which protected the immobilized GOx–chitosan– multi-walled carbon nanotube (MWCNT) matrix while allowing unhindered diffusion of small molecules.[74] The three-electrode system consisted of an electroplated Au counter electrode, an Ag/AgCl reference electrode stabilized with a PVB–KCl cocktail, and a working electrode incorporating the nanostructured enzyme matrix (Fig. 3B). Morphological analysis confirmed the functional layering of the working electrode (Fig. 3C): a transducer membrane on the Au substrate, the GOx–MWCNT– chitosan matrix, and the crosslinked protective coating. FE-SEM imaging revealed a porous and interconnected MWCNT network that facilitated efficient electron transport, thereby enhancing sensitivity.[75] The calibration setup is shown in Fig. 3D, with electrodes immersed in phosphate-buffered saline (PBS, 1×) containing glucose at varying concentrations. Chronoamperometric measurements (Fig. 3E) demonstrated stepwise increases in current magnitude as the glucose concentration increased from 0.01 to 25 mM. Transient responses were further analyzed by Cottrell plots (Fig. 3F), which exhibited linear dependence of current on $t^{-0.5}$, confirming the diffusion-controlled kinetics of glucose transport and oxidation.[76] Real-time chronoamperometric traces under sequential glucose additions are shown in Fig. 3G. Each spike produced discrete current steps with a rapid response time of less than a second, as highlighted in the inset, reflecting both efficient diffusion through the protective coating and rapid catalytic turnover of the immobilized enzyme. From these responses, a calibration curve was constructed (Fig. 3H), revealing an excellent linear relationship between steady-state current and glucose concentration across a wide dynamic range (0.01–25 mM, $R^2 = 0.9985$). The calculated sensitivity was 15.48 μA mM^{-1} cm^{-2}, with a detection limit of ∼42 μM (S/N = 3), sufficient to cover physiological salivary glucose concentrations.

Given that normal salivary glucose levels rarely exceed 1 mM, we further replotted the calibration curve over the physiologically relevant low concentration range (Fig. 3I).[77] Within this range, the sensor maintained excellent repeatability. Importantly, the sensor exhibited negligible baseline drift and superior reproducibility compared to the reference, validating its applicability for continuous monitoring of salivary glucose. These results demonstrate that the integration of a nanostructured enzyme layer, stabilized reference electrode, and protective crosslinked coating enables highly sensitive, diffusion-controlled, and physiologically relevant detection of salivary glucose, establishing its reliability for continuous intraoral monitoring applications.

Retainer microfluidic system enabling capillary saliva flow and real-time functionality

Microfluidic channels were fabricated within the optimized 3.0 wt% PDMS–(PDMS-b-PEO) composite films using successive laser pyrolysis (SLP), a direct-write technique that enables high-resolution patterning without the use of photolithography.[78] The SLP process was initiated by marking the laser entry point with opaque ink to induce initial pyrolysis, producing an opaque SiC by-product that more effectively absorbs photothermal energy, leading to continuous irradiation along the scanning path.[79] Debris removal was accomplished by ultrasonication in isopropyl alcohol, yielding clean channels with minimal surface roughness. No additional O_2 plasma treatment was performed. As shown in Fig. 4A, the patterned films exhibited smooth, well-defined channel structures that were mechanically flexible yet dimensionally stable, allowing for straightforward handling and integration into the retainer architecture. The fabrication sequence was captured in real time and is provided in Movie S3, where the successive propagation of the pyrolysis front can be seen. A schematic of the channel fabrication principle and representative images of patterned structures are shown in Fig. 4B. The diagram illustrates the sequential steps of (1) laser pyrolysis initiation, (2) debris removal, and (3) completed microchannel formation (Fig. S6). The profile data of the inlet and channel pathways are provided in Fig. S7 and S8, while various hatch designs that were tested to form the reservoir are shown in Fig. S9. Time-lapse images in Fig. 4C further demonstrate capillary-driven filling of the channels using dyed artificial saliva. Within seconds of introducing a small droplet at the inlet, the channels filled uniformly without the need for external pumping, validating the persistent hydrophilicity imparted by the PDMS-b-PEO modification. Notably, spontaneous filling occurred within approximately 60 seconds for a 30 μL input volume, and the flow front advanced smoothly without bubble entrapment or discontinuities. To validate integration with the retainer platform, the patterned films were bonded into recessed grooves of the 3D-printed resin retainer base. Fig. 4D shows the assembled prototype positioned within a custom-built artificial saliva chamber. This configuration enabled a direct connection between the oral-mimicking fluid reservoir and the sensor-embedded retainer system. Fig. 4E presents calibration curves obtained by preparing glucose stock solutions in two different media, PBS and artificial saliva. Noticeable current differences were observed at identical glucose concentrations, attributable to several physicochemical factors, such as higher viscosity and additive content of artificial saliva which reduced the diffusion coefficient (D) of H_2O_2 (e.g., $D_{H_2O_2} \approx 1.4 \times 10^{-9}$ m^2 s^{-1} in water and $\approx 0.9 \times 10^{-9}$ m^2 s^{-1} in artificial saliva) and other electroactive species, thereby lowering the diffusion-limited current.[80–83] Fig. 4F illustrates chronoamperometric responses under repeated glucose injections in artificial saliva flow. Since sucrose, a common dietary sugar, is not enzymatically hydrolyzed into glucose within the oral cavity, glucose solutions were directly introduced at physiologically relevant levels (10 mM) to mimic transient salivary glucose spikes. Between glucose injections, only artificial saliva was supplied, providing a stable baseline. Upon each glucose pulse, the sensor exhibited sharp, reproducible transient current increases with negligible
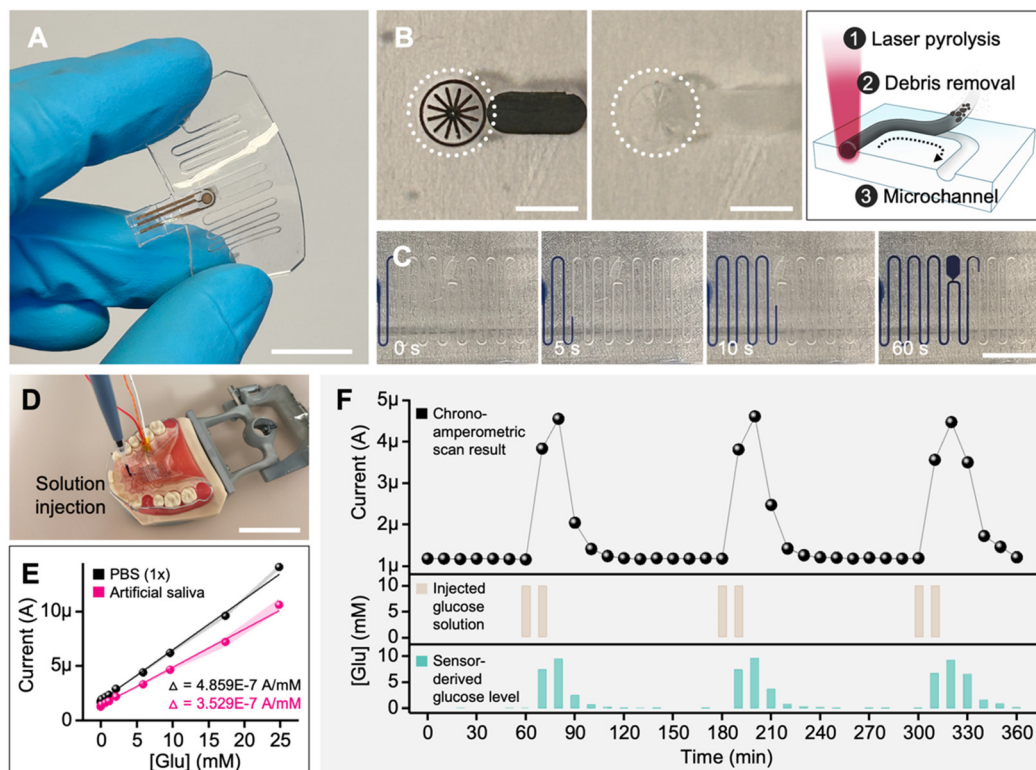
Fig. 4 Characterization and integration of sensor-embedded microfluidic channels for saliva glucose monitoring. (A) PDMS–(PDMS-*b*-PEO) microchannel patterned by successive laser pyrolysis (SLP), showing a well-defined geometry and smooth sidewalls. Scale bar = 10 mm. (B) Saliva inlet before/after debris removal by ultrasonication in isopropyl alcohol, illustrating effective elimination of residues at the entry. Scale bar = 3 mm. (C) Time-lapse capillary filling with blue-dyed artificial saliva, demonstrating spontaneous and uniform wicking along the channel. Scale bar = 5 mm. (D) Photograph of the electrochemical measurement setup: retainer prototype with three-electrode connections, inlet reservoir, vents, and cellulose wicking outlet. Scale bar = 30 mm. (E) Calibration plot of the sensor response *versus* glucose concentration in PBS (1×) and artificial saliva, respectively. (F) Representative 6 h continuous chronoamperometric trace (interval: 10 min) under artificial saliva flow: glucose solution injections (beige bars) and sensor-derived glucose concentrations (cyan bars) inferred from the recorded current.

baseline drift, confirming high repeatability across three consecutive injections. An expanded view of baseline chronoamperometric currents under continuous artificial saliva flow is shown in Fig. S10, where artificial saliva alone (black trace) is contrasted with glucose-spiked saliva (cyan trace). The sensor consistently produced stable current baselines and rapid responses to glucose additions, demonstrating that capillary-driven flow was sufficient to sustain continuous sample delivery to the sensing interface. The glucose sensor also shows stable performance over extended operation for 6 hours without measurable degradation (Fig. 4F). In addition, a 7 day storage-stability test showed no significant changes in the current level or calibration slope, indicating that the GOx–MWCNT–chitosan electrode retains its activity during short-term refrigerated storage. Selectivity tests performed in artificial saliva with physiologically relevant concentrations of creatinine, uric acid, and ascorbic acid demonstrated negligible interference, confirming that the sensor maintains high biochemical specificity consistent with GOx-based systems (Fig. S11). These results collectively confirm that successive laser pyrolysis enables reproducible fabrication of hydrophilic PDMS–(PDMS-*b*-PEO) microchannels that integrate seamlessly with

orthodontic retainer substrates. The combination of rapid capillary flow, stable electrochemical responses, and compatibility with artificial saliva chambers demonstrates the feasibility of this system as a functional prototype for continuous intraoral glucose monitoring. Because the intraoral retainer is worn in a mechanically stable configuration with minimal bending during normal use, the glucose electrode experiences limited deformation. Prior studies on GOx-based flexible electrochemical sensors have shown stable performance under large bending, twisting, and even stretching strains, indicating that thin-film Au/MWCNT/chitosan electrodes such as ours are inherently tolerant to mechanical stress.[84–88] Systematic mechanical cycling tests will be incorporated in the next-stage integrated retainer system. Consistent with the trajectory proposed in recent reviews on noninvasive glucose sensing,[33–35] subsequent work will include *in vivo* evaluations to establish quantitative correlations between salivary and blood glucose levels, assess long-term biofouling and in-mouth bacterial contamination, and benchmark the retainer-based platform against clinical CGM and blood-glucose measurements. To contextualize the performance of our retainer-based platform, we compared its characteristics with those of previously reported microfluidic

Table 1 Comparison of reported microfluidic electrochemical biosensing systems for human saliva monitoring

Ref.	Device type	Target biomarker	Hydrophilic strategy	Stability (days) in saliva	Hydrophobic recovery (days)	Continuous monitoring
This study	Retainer	Glucose	PDMS-b-PEO blending	>90 (validated)	>120 (no recovery observed)	Yes (validated: 6 h)
89	Pacifier	Na^+, K^+	PEG blending	~1	<3	Yes (60 min)
90	Dental floss	Cortisol	Plasma-treated fiber	<1	N/A	No
91	Cotton swab + PDMS chip	Cotinine	Magnetic bonding	~14 (humid, 4 °C)	N/A	No
92	Mouthguard	Glucose, nitrite	Disposable colorimetric	<1 (40 s use)	N/A	No
93	Wearable sensor array	Na^+, H^+, and uric acid	N/A	N/A	N/A	Yes (90 min)
94	Thin-film membrane	Glucose, alcohol	O_2 plasma treatment	N/A	N/A	Yes (24 h)
95	Disposable flow-cell	Carbamazepine (drug)	N/A	N/A (measurement made in 2 min)	N/A	No

electrochemical biosensing systems for salivary monitoring (Table 1).

Various device formats have been explored, ranging from pacifier-like holders and dental floss threads to mouthguards and modular chips.[89,90,92,96] While these approaches demonstrate ingenuity in leveraging oral-accessible substrates, most are hindered by the transient hydrophilicity of PDMS channels, short-term stability (<1 day), or limited compatibility with continuous in-mouth wear. For instance, PDMS–PEG or plasma-treated surfaces can initially promote saliva wicking, but hydrophobic recovery typically occurs within days, reducing their reliability for long-term deployment. Similarly, cotton- or paper-based microfluidics provide simple saliva sampling but lack durability, precise channel definition, and full integration with solid-state electrochemical sensors.[97] In contrast, our system combines a PDMS–(PDMS-b-PEO) composite that sustains superhydrophilicity for more than 120 days with a seamlessly embedded enzymatic sensor in a retainer-compatible format. This approach enables stable capillary-driven saliva transport without recurrent surface treatment, robust electrochemical performance with high sensitivity and a low detection limit (~42 μM), and real-time responsiveness to dynamic glucose fluctuations. Importantly, the retainer geometry ensures ergonomic fit, unobtrusive wear, and compatibility with long-term intraoral operation—features rarely achieved in earlier studies. Collectively, this positions our device as a step-change advancement toward practical, non-invasive, and continuous salivary glucose monitoring in daily-life settings.

Conclusions

In this study, we report a retainer-based microfluidic platform for continuous salivary glucose monitoring, integrating a hydrophilically modified polymer substrate and a nanostructured sensor. The incorporation of PDMS-b-PEO into PDMS offers long-lasting surface hydrophilicity while preserving mechanical elasticity and dimensional stability. Optimization experiments identified 3.0 wt% PEO as the ideal composition, enabling contact angles below 20° sustained over 120 days, with negligible compromise in tensile performance. These properties provided a robust foundation for constructing stable

microfluidic channels suitable for intraoral use. The integrated glucose sensor demonstrates high sensitivity and rapid responsiveness across a physiologically relevant range. Importantly, calibration curves remained linear over both broad (0.01–25 mM) and physiologically relevant low-concentration ranges (<1 mM). The microfluidic channels support the capillary-driven flow of artificial saliva, achieving complete filling within seconds and ensuring stable delivery to the sensing interface. *In vitro* experiments using a custom-built saliva chamber validate the continuous monitoring capability of the system, which reliably tracks dynamic changes in glucose concentration. Collectively, the class of technologies, including durable hydrophilic composites, enzymatic electrochemical sensors, and laser-patterned microchannels, shows the potential of this integrated system for non-invasive, continuous salivary glucose monitoring.

Author contributions

Jimin Lee: conceptualization, methodology, investigation, data curation, visualization, writing – original draft, writing – review & editing. JunHo Song: methodology, formal analysis, software, validation, writing – original draft. Juo Kim: methodology, formal analysis, software, writing – original draft. Arianna Lee: investigation, writing – original draft, writing – review & editing. Saewoong Oh: investigation. Beomjune Shin: investigation. Kyoungmin Min: supervision, writing – review & editing. Woon-Hong Yeo: funding acquisition, supervision, resources, writing – review & editing.

Conflicts of interest

Georgia Tech has a pending US patent application regarding the materials in this paper.

Data availability

The data supporting this article have been included as part of the supplementary information (SI).

Supplementary information is available. See DOI: https://doi.org/10.1039/d5lc00934k.

Acknowledgements

Notes and references

1 B. B. Duncan, D. J. Magliano and E. J. Boyko, *IDF diabetes atlas 11th edition 2025: global prevalence and projections for 2050, Report 0931-0509*, 2025.

2 M. J. Fowler, *Clin. Diabetes*, 2011, **29**, 116–122.

3 M. E. Hilliard, W. Levy, B. J. Anderson, A. L. Whitehouse, P. V. Commissariat, K. R. Harrington, L. M. Laffel, K. M. Miller, M. Van Name, W. V. Tamborlane, D. J. DeSalvo and L. A. DiMeglio, *Diabetes Technol. Ther.*, 2019, **21**, 493–498.

4 N. A. M. Asarani, A. N. Reynolds, S. E. Boucher, M. de Bock and B. J. Wheeler, *J. Diabetes Sci. Technol.*, 2020, **14**, 328–337.

5 B. E. Marks and J. I. Wolfsdorf, *Front. Endocrinol.*, 2020, **11**, 2020.

6 W. Villena Gonzales, A. T. Mobashsher and A. Abbosh, *Sensors*, 2019, **19**, 800.

7 C. Jurysta, N. Bulur, B. Oguzhan, I. Satman, T. M. Yilmaz, W. J. Malaisse and A. Sener, *BioMed Res. Int.*, 2009, **2009**, 430426.

8 A. S. Panchbhai, *J. Oral Maxillofac. Surg.*, 2012, **3**, e3.

9 Y. Cui, H. Zhang, J. Zhu, Z. Liao, S. Wang and W. Liu, *Int. J. Environ. Res. Public Health*, 2022, **19**, 4122.

10 X. Zhang, F. Li, A. N. Nordin, J. Tarbell and I. Voiculescu, *Sens. Bio-Sens. Res.*, 2015, **3**, 112–121.

11 J. M. Goodson, M.-L. Hartman, P. Shi, H. Hasturk, T. Yaskell, J. Vargas, X. Song, M. Cugini, R. Barake, O. Alsmadi, S. Al-Mutawa, J. Ariga, P. Soparkar, J. Behbehani and K. Behbehani, *PLoS One*, 2017, **12**, e0170437.

12 J. Lee, M. C. Kim, I. Soltis, S. H. Lee and W.-H. Yeo, *Adv. Sens. Res.*, 2023, **2**, 2200088.

13 I. Wong and C.-M. Ho, *Microfluid. Nanofluid.*, 2009, **7**, 291–306.

14 S. Halldorsson, E. Lucumi, R. Gómez-Sjöberg and R. M. T. Fleming, *Biosens. Bioelectron.*, 2015, **63**, 218–231.

15 I. Miranda, A. Souza, P. Sousa, J. Ribeiro, E. M. S. Castanheira, R. Lima and G. Minas, *J. Funct. Biomater.*, 2022, **13**, 2.

16 L. B. Neves, I. S. Afonso, G. Nobrega, L. G. Barbosa, R. A. Lima and J. E. Ribeiro, *Micromachines*, 2024, **15**, 670.

17 J. Zhou, A. V. Ellis and N. H. Voelcker, *Electrophoresis*, 2010, **31**, 2–16.

18 H. Madadi and J. Casals-Terré, *Microsyst. Technol.*, 2013, **19**, 143–150.

19 E. Holczer and P. Fürjes, *Microfluid. Nanofluid.*, 2017, **21**, 81.

20 T. Shimada, K. Fujino, T. Yasui, N. Kaji, Y. Ueda, K. Fujii, H. Yukawa and Y. Baba, *Anal. Chem.*, 2023, **95**, 18335–18343.

21 M. Fukuyama, M. Tokeshi, M. A. Proskurnin and A. Hibara, *Lab Chip*, 2018, **18**, 356–361.

22 S. Yang, Q. Xian, Y. Liu, Z. Zhang, Q. Song, Y. Gao and W. Wen, *J. Funct. Biomater.*, 2023, **14**, 208.

23 D. B. Mair, M. A. C. Williams, J. F. Chen, A. Goldstein, A. Wu, P. H. U. Lee, N. J. Sniadecki and D.-H. Kim, *ACS Appl. Mater. Interfaces*, 2022, **14**, 38541–38549.

24 T. Trantidou, Y. Elani, E. Parsons and O. Ces, *Microsyst. Nanoeng.*, 2017, **3**, 16091.

25 L. Yu, C. M. Li, Q. Zhou and J. H. T. Luong, *Bioconjugate Chem.*, 2007, **18**, 281–284.

26 Y. A. Alzahid, P. Mostaghimi, A. Gerami, A. Singh, K. Privat, T. Amirian and R. T. Armstrong, *Sci. Rep.*, 2018, **8**, 15518.

27 Z. Wu and K. Hjort, *Lab Chip*, 2009, **9**, 1500–1503.

28 A. Kamnerdsook, E. Juntasaro, N. Khemthongcharoen, M. Chanasakulniyom, W. Sripumkhai, P. Pattamang, C. Promptmas, N. Atthi and W. Jeamsaksiri, *RSC Adv.*, 2021, **11**, 35653–35662.

29 K. Zhou, M. Dey, B. Ayan, Z. Zhang, V. Ozbolat, M. H. Kim, V. Khristov and I. T. Ozbolat, *Biomed. Mater.*, 2021, **16**, 045005.

30 J. G. Alauzun, S. Young, R. D'Souza, L. Liu, M. A. Brook and H. D. Sheardown, *Biomaterials*, 2010, **31**, 3471–3478.

31 M. A. J. Mazumder, *Arabian J. Sci. Eng.*, 2017, **42**, 271–280.

32 D. Yin, A. Shi, B. Zhou, M. Wang, G. Xu, M. Shen, X. Zhu and X. Shi, *Langmuir*, 2022, **38**, 11080–11086.

33 T. Saha, R. Del Caño, K. Mahato, E. De la Paz, C. Chen, S. Ding, L. Yin and J. Wang, *Chem. Rev.*, 2023, **123**, 7854–7889.

34 H. Teymourian, A. Barfidokht and J. Wang, *Chem. Soc. Rev.*, 2020, **49**, 7671–7709.

35 T. Saha, M. I. Khan, S. S. Sandhu, L. Yin, S. Earney, C. Zhang, O. Djassemi, Z. Wang, J. Han, A. Abdal, S. Srivatsa, S. Ding and J. Wang, *Adv. Sci.*, 2024, **11**, 2405518.

36 S. Plimpton, *J. Comput. Phys.*, 1995, **117**, 1–19.

37 A. Gökaltun, Y. B. Kang, M. L. Yarmush, O. B. Usta and A. Asatekin, *Sci. Rep.*, 2019, **9**, 7377.

38 S. Hosseini, H. Savaloni and M. Gholipour Shahraki, *Appl. Surf. Sci.*, 2019, **485**, 536–546.

39 S. K. Sethi, L. Soni, U. Shankar, R. P. Chauhan and G. Manik, *J. Mol. Struct.*, 2020, **1202**, 127342.

40 B. Jiang, H. Guo, D. Chen and M. Zhou, *Appl. Surf. Sci.*, 2022, **574**, 151704.

41 Y. Zhang, Y. Zhu, G. Lin, R. S. Ruoff, N. Hu, D. W. Schaefer and J. E. Mark, *Polymer*, 2013, **54**, 3605–3611.

42 C.-E. Fang, Y.-C. Tsai, C. Scheurer and C.-C. Chiu, *Polymer*, 2021, **13**, 1131.

43 W. L. Jorgensen, D. S. Maxwell and J. Tirado-Rives, *J. Am. Chem. Soc.*, 1996, **118**, 11225–11236.

44 Z. Xiang, C. Gao, T. Long, L. Ding, T. Zhou and Z. Wu, *J. Phys. Chem. B*, 2025, **129**, 1864–1873.

45 H. J. C. Berendsen, J. R. Grigera and T. P. Straatsma, *J. Phys. Chem.*, 1987, **91**, 6269–6271.

46 D. Boda and D. Henderson, *Mol. Phys.*, 2008, **106**, 2367–2370.

47 Y. Yin, W. Li, H. Shen, J. Zhou, H. Nan, M. Deng, X. Shen and Z. Tu, *ISIJ Int.*, 2018, **58**, 1022–1027.

48 N. Archer, S. A. Ladan, H. T. Lancashire and H. Petridis, *Oral*, 2024, **4**, 148–162.

49 Ž. V. Popović, A. Thiha, F. Ibrahim, B. B. Petrović, N. A. Dahlan, L. Milić, S. Kojić and G. M. Stojanović, *Sci. Rep.*, 2023, **13**, 21277.

50 J. Timpel, S. Klinghammer, L. Riemenschneider, B. Ibarlucea, G. Cuniberti, C. Hannig and T. Sterzenbach, *Clin. Oral Investig.*, 2023, **27**, 5719–5736.

51 M. Dewan, D. Shrivastava, L. Goyal, A. Zwiri, A. F. Hussein, M. K. Alam, K. C. Srivastava and S. Anil, *Eur. J. Dent.*, 2024, **19**, 286–297.

52 R. Park, S. Jeon, J. Jeong, S.-Y. Park, D.-W. Han and S. W. Hong, *Biosensors*, 2022, **12**, 136.

53 J. Wang, J. Yu, T. Wang, C. Li, Y. Wei, X. Deng and X. Chen, *J. Mater. Chem. B*, 2020, **8**, 3341–3356.

54 J. Tu, R. M. Torrente-Rodríguez, M. Wang and W. Gao, *Adv. Funct. Mater.*, 2020, **30**, 1906713.

55 Y. Lee, C. Howe, S. Mishra, D. S. Lee, M. Mahmood, M. Piper, Y. Kim, K. Tieu, H.-S. Byun, J. P. Coffey, M. Shayan, Y. Chun, R. M. Costanzo and W.-H. Yeo, *Proc. Natl. Acad. Sci. U. S. A.*, 2018, **115**, 5377–5382.

56 J. C. McDonald and G. M. Whitesides, *Acc. Chem. Res.*, 2002, **35**, 491–499.

57 A. Mata, A. J. Fleischman and S. Roy, *Biomed. Microdevices*, 2005, **7**, 281–293.

58 K. Efimenko, W. E. Wallace and J. Genzer, *J. Colloid Interface Sci.*, 2002, **254**, 306–315.

59 H. Hillborg and U. W. Gedde, *Polymer*, 1998, **39**, 1991–1998.

60 M. Yao and J. Fang, *J. Micromech. Microeng.*, 2012, **22**, 025012.

61 M. Yao, G. Shah and J. Fang, *Micromachines*, 2012, **3**, 462–479.

62 D. Bodas and C. Khan-Malek, *Sens. Actuators, B*, 2007, **123**, 368–373.

63 J. Yang, Z. Zhai, J. Liu and C. Weng, *J. Appl. Polym. Sci.*, 2021, **138**, 50105.

64 K. Tasaki, *J. Am. Chem. Soc.*, 1996, **118**, 8459–8469.

65 J. A. González Calderón, D. Contreras López, E. Pérez and J. Vallejo Montesinos, *Polym. Bull.*, 2020, **77**, 2749–2817.

66 R. Ariati, F. Sales, A. Souza, R. A. Lima and J. Ribeiro, *Polymer*, 2021, **13**, 4258.

67 J. Smith, *PhD*, Loughborough University, 2021, DOI: 10.26174/thesis.lboro.14416346.v1.

68 Y. Maslii, N. Herbina, L. Dene, L. Ivanauskas, G. Matulis and J. Bernatoniene, *Pharm. Dev. Technol.*, 2025, **30**, 505–520.

69 G. C. Yeo, B. Aghaei-Ghareh-Bolagh, E. P. Brackenreg, M. A. Hiob, P. Lee and A. S. Weiss, *Adv. Healthcare Mater.*, 2015, **4**, 2530–2556.

70 L. V. Parfenova, Z. R. Galimshina and E. V. Parfenov, *Int. J. Mol. Sci.*, 2024, **25**, 11623.

71 J. Lee, H. Kim, H.-R. Lim, Y. S. Kim, T. T. T. Hoang, J. Choi, G.-J. Jeong, H. Kim, R. Herbert, I. Soltis, K. R. Kim, S. H. Lee, Y. Kwon, Y. Lee, Y. C. Jang and W.-H. Yeo, *Sci. Adv.*, 2024, **10**, eadk6714.

72 N. Mohamad Nor, N. S. Ridhuan and K. Abdul Razak, *Biosensors*, 2022, **12**, 1136.

73 D. R. Bagal-Kestwal and B.-H. Chiang, *Polymer*, 2019, **11**, 1958.

74 W. Lipińska, K. Siuzdak, J. Karczewski, A. Dołęga and K. Grochowska, *Sens. Actuators, B*, 2021, **330**, 129409.

75 F. N. Comba, M. R. Romero, F. S. Garay and A. M. Baruzzi, *Anal. Biochem.*, 2018, **550**, 34–40.

76 K. Phasuksom and A. Sirivat, *RSC Adv.*, 2022, **12**, 28505–28518.

77 S. Wang, T. Chinnasamy, M. A. Lifson, F. Inci and U. Demirci, *Trends Biotechnol.*, 2016, **34**, 909–921.

78 K. Min, J. Lim, J. H. Lim, E. Hwang, Y. Kim, H. Lee, H. Lee and S. Hong, *Materials*, 2021, **14**, 7275.

79 J. Shin, J. Ko, S. Jeong, P. Won, Y. Lee, J. Kim, S. Hong, N. L. Jeon and S. H. Ko, *Nat. Mater.*, 2021, **20**, 100–107.

80 A. Rabti, W. Argoubi and N. Raouafi, *Microchim. Acta*, 2016, **183**, 1227–1233.

81 P. A. Raymundo-Pereira, F. M. Shimizu, D. Coelho, M. H. O. Piazzeta, A. L. Gobbi, S. A. S. Machado and O. N. Oliveira, *Biosens. Bioelectron.*, 2016, **86**, 369–376.

82 J. Liu, S. Sun, H. Shang, J. Lai and L. Zhang, *Electroanalysis*, 2016, **28**, 2016–2021.

83 E. Gričar, K. Kalcher, B. Genorio and M. Kolar, *Sensors*, 2021, **21**, 8301.

84 M.-C. Chuang, Y.-L. Yang, T.-F. Tseng, T. Chou, S.-L. Lou and J. Wang, *Talanta*, 2010, **81**, 15–19.

85 A. J. Bandodkar, I. Jeerapan, J.-M. You, R. Nuñez-Flores and J. Wang, *Nano Lett.*, 2016, **16**, 721–727.

86 J. Madden, E. Vaughan, M. Thompson, A. O'Riordan, P. Galvin, D. Iacopino and S. Rodrigues Teixeira, *Talanta*, 2022, **246**, 123492.

87 H. Lee, T. K. Choi, Y. B. Lee, H. R. Cho, R. Ghaffari, L. Wang, H. J. Choi, T. D. Chung, N. Lu, T. Hyeon, S. H. Choi and D.-H. Kim, *Nat. Nanotechnol.*, 2016, **11**, 566–572.

88 J. Cai, K. Cizek, B. Long, K. McAferty, C. G. Campbell, D. R. Allee, B. D. Vogt, J. La Belle and J. Wang, *Sens. Actuators, B*, 2009, **137**, 379–385.

89 H.-R. Lim, S. M. Lee, S. Park, C. Choi, H. Kim, J. Kim, M. Mahmood, Y. Lee, J.-H. Kim and W.-H. Yeo, *Biosens. Bioelectron.*, 2022, **210**, 114329.

90 A. Sharma, N. I. Hossain, A. Thomas and S. Sonkusale, *ACS Appl. Mater. Interfaces*, 2025, **17**, 25083–25096.

91 K. Lee, T. Yoon, H.-S. Yang, S. Cha, Y.-P. Cheon, L. Kashefi-Kheyrabadi and H.-I. Jung, *Lab Chip*, 2020, **20**, 320–331.

92 L. F. de Castro, S. V. de Freitas, L. C. Duarte, J. A. C. de Souza, T. R. L. C. Paixão and W. K. T. Coltro, *Anal. Bioanal. Chem.*, 2019, **411**, 4919–4928.

93 Y. Bi, M. Sun, J. Wang, Z. Zhu, J. Bai, M. Y. Emran, A. Kotb, X. Bo and M. Zhou, *Anal. Chem.*, 2023, **95**, 6690–6699.

94 F. Wang, C. Song, Y. Li, H. Yang, D. Yang, K. Chen, L. Xiang, C. Hong, R. Cai and W. Tan, *Nano Lett.*, 2025, **25**, 9853–9862.

95 L. Wentland, J. M. Cook, J. Minzlaff, S. A. Ramsey, M. L. Johnston and E. Fu, *J. Appl. Electrochem.*, 2023, **53**, 523–534.

96 B. Liang, S. Wang, J. Zheng, B. Li, N. Cheng and N. Gan, *Biosens. Bioelectron.*, 2025, **271**, 117077.

97 X. Li, S. You, Z. Fan, G. Li and L. Fu, *Sens. Rev.*, 2024, **44**, 35–67.